

Thermal and Nonthermal X-ray Emission from the Forward Shock in Tycho's Supernova Remnant

Una Hwang (1,2), Anne Decourchelle (3), Stephen S. Holt (4), and Robert Petre (1)

(1) *NASA Goddard Space Flight Center, Greenbelt, MD 20771*

(2) *Department of Astronomy, University of Maryland, College Park, MD 20742*

(3) *Service d'Astrophysique, CEA Saclay, 91191 Gif-sur-Yvette Cedex, France*

(4) *F. W. Olin College of Engineering, Needham, MA 02492*

ABSTRACT

We present Chandra X-ray images of Tycho's supernova remnant that delineate its outer shock as a thin, smooth rim along the straight northeastern edge and most of the circular western half. The images also show that the Si and S ejecta are highly clumpy, and have reached near the forward shock at numerous locations. Most of the X-ray spectra that we examine along the rim show evidence of line emission from Si and S ejecta, while the continuum is well-represented by either a thermal or nonthermal model. If the continuum is assumed to be thermal, the electron temperatures at the rim are all similar at about 2 keV, while the ionization ages are very low, because of the overall weakness of the line emission. These electron temperatures are substantially below those expected for equilibration of the electron and ion temperatures, assuming shock velocities inferred from radio and X-ray expansion measurements; the electron to mean temperature ratios are $\lesssim 0.1 - 0.2$, indicating that collisionless heating of the electrons at the shock is modest. The nonthermal contribution to these spectra may be important, but cannot be strongly constrained by these data. It could account for as much as half of the flux in the 4-6 keV energy range, based on an extrapolation of the hard X-ray spectrum above 10 keV.

Subject headings: supernova remnants—ISM:individual(Tycho's SNR)—X-rays:general

1. Introduction

As the bright remnant of an historically observed supernova in our Galaxy, Tycho's supernova remnant (SNR 1572) has been extensively studied, but the X-ray spectrum associated with its forward shock has not been directly measured until now. By necessity, most

X-ray spectral studies have focused on the spatially integrated spectrum, which is dominated at energies below a few keV by the ejecta. A faint outer shelf of emission was identified in X-ray images from the Einstein Observatory, however, and is attributed to material behind the forward shock (Seward, Gorenstein, & Tucker 1983)—an association that is further supported by the excellent correspondence of the X-ray boundary with the sharp outer boundary seen in radio images (Dickel et al. 1991).

Imaging studies with the ROSAT X-ray Observatory establish that the expansion of the remnant varies both with azimuthal angle and radius (Hughes 2000). The faster expansion observed at the outer boundary corresponds to an average forward shock velocity of 4600 ± 400 ($D/2.3$ kpc) km/s, where D is the distance in kpc. The expansion of the radio boundary is also observed to vary with azimuthal angle (Strom, Goss, & Shaver 1982, Reynoso et al. 1997). Strong deceleration in the east is caused by the remnant’s interaction with dense H gas (Reynoso et al. 1999). Although the outer boundaries of the X-ray and radio emission show excellent correspondence, the average expansions measured at these wavelengths are inconsistent: the expansion rate m , defined such that the time evolution of the remnant radius is $r \sim t^m$, is 0.471 ± 0.028 in the radio (Reynoso et al. 1997), and 0.71 ± 0.06 for the outer radii in X-rays (Hughes 2000). This discrepancy is unresolved, but appears to be a common pattern in young remnants (such as Cas A, Koralesky et al. 1998, Vink et al. 1998, and Kepler’s SNR, Dickel et al. 1988, Hughes 1999).

In the case of Tycho’s SNR, the forward shock velocity can be measured in yet another way. The optical emission is almost exclusively H Balmer emission from nonradiative shocks propagating into partially neutral gas (Chevalier & Raymond 1978, Chevalier, Kirshner, & Raymond 1980, Kirshner, Winkler, & Chevalier 1987). The neutral H atoms are not heated by the shock, and can be collisionally excited before being ionized; these excited atoms produce narrow Balmer lines consistent with their low temperatures. Slow H atoms can also undergo charge exchange reactions with fast protons that have already been heated behind the shock; these fast H atoms contribute a broad component to the line profile. The optical emission from Tycho’s SNR is generally faint, and is detected only in the eastern and northern regions. The most prominent feature is on the eastern side of the remnant (knot g in the compilation of Kamper & van den Bergh 1978). Smith et al. (1991) and Ghavamian et al. (2001) infer shock velocities through knot g of ~ 2000 km/s independent of the distance to the remnant. From modelling the line emission, while accounting for the effects of both the electron-ion temperature equilibration and Ly α scattering, Ghavamian et al. constrain the electron to proton temperature ratio to be $\lesssim 0.10$, implying electron temperatures $\lesssim 0.8$ keV in the knot.

X-ray spectral studies of Tycho’s SNR generally infer a relatively hard spectral com-

ponent, presumed to be associated with the forward shock. The total spectrum from the Advanced Satellite for Cosmology and Astrophysics (ASCA) X-ray Observatory suggests a forward shock component with a temperature of roughly 4 keV that accounts for some 30% of the X-ray flux between 0.5 to 10 keV (Hwang, Hughes, & Petre 1998). This temperature is well below the mean equilibrium temperature behind a 4600 km/s shock. Hughes (2000) points out that this implies either a low efficiency for electron heating, so that the electron temperature is well below the mean, or nonlinear particle acceleration, which could result in significantly higher compressions and lower temperatures than for test-particle shocks of the same velocity (Decourchelle, Ellison & Ballet 2000). Furthermore, X-ray emission has been observed from the remnant at energies up to 25 keV (Pravdo & Smith 1979, Fink et al. 1988, Petre et al. 1999), and this emission has also been attributed to material behind the forward shock. This interpretation requires a heating mechanism that can rapidly heat the electrons to sufficiently high temperatures (e.g., Cargill & Papadopoulos 1988). The hard X-ray emission has alternatively been suggested to come from a nonthermal population of highly energetic electrons that have been accelerated at the shock (Aharonian et al. 2001).

X-ray instruments have lacked the capability to isolate the spectrum of the forward shock thus far. Recent XMM-Newton observations have now provided the first truly spatially resolved spectra of Tycho’s SNR on angular scales of several arcseconds (Decourchelle et al. 2001). Even higher spatial resolution (less than 0.5'' FWHM) is provided by the Chandra X-ray Observatory. In this paper, we present images and spectra of selected portions of the forward shock of Tycho’s SNR using the Advanced CCD Imaging Spectrometer (ACIS) on the Chandra Observatory.

2. Images

Tycho’s SNR was observed for 48.9 ks on 20-21 September 2000 with the ACIS spectroscopic array. The count rate was steady, and there were no background flares. The remnant has a size slightly larger than the $8' \times 8'$ field of view of a single ACIS CCD. The northern and eastern parts of the remnant were positioned on the back-illuminated CCD S3, the primary spectroscopic chip, while the western region of the remnant was imaged on the neighbouring front-illuminated CCD S2. This placement of the source on the detector was originally chosen to optimize observation of the ejecta knots in the east. The southernmost region of the remnant fell outside the field of view of the detector.

The broadband 0.5-10 keV image of Tycho’s SNR obtained by ACIS is shown in Figure 1(a). Also shown in Figure 1 are energy band images covering (b) the Si He α blend near 1.86 keV, with the underlying continuum subtracted, and (c) the 4-6 keV continuum band. In

forming the X-ray images, the energy selection was performed after correcting for the spatial variation of the gain across the detector, as summarized in Table 1. For the Si image, the continuum underlying the line emission was determined from the shape of the local spectrum, and removed. The rather sparse 4–6 keV continuum image has been smoothed. Panel (d) shows the 22 cm radio image of Dickel et al. (1991), convolved with a beam of $1.45'' \times 1.38''$. “Equivalent width” images of the kind presented by Hwang et al. (2000) are shown in the three panels of Figure 2 for (a) the Fe L emission (transitions to $n=2$ levels) near 1 keV, (b) Si He α blend, and (c) the Fe K blend (transitions to $n=1$ levels) near 6.5 keV. These images show the ratio of the line emission to the underlying continuum after smoothing.

2.1. Outer Shock

The Chandra broadband image shows that the outer edge of the X-ray emission in the northeast and west is strikingly traced by a thin, smooth rim. The rim is circular in the west, but there is a straight section in the northeast, and the rim is absent altogether in the east, where the remnant is interacting with dense H gas (Reynoso et al. 1999). The rim is also present at radio wavelengths, where it extends to the southern edge of the remnant that was not imaged by this Chandra observation (Figure 1d, Dickel et al. 1991, Reynoso et al. 1997). Overall, the radio rim corresponds closely with the X-ray rim, but the two do not track each other particularly well in brightness, as illustrated in Figure 3, which compares the surface brightness along the rim in the X-ray continuum image with that in the radio image (also see Dickel et al. 1991).

X-ray radial profiles for two azimuthal sectors in the northwest and southwest are shown in Figure 4 for both the broadband and 4–6 keV continuum images. The rim marks the location of the remnant’s forward shock, and is highlighted in the 4–6 keV X-ray continuum image. This energy band suppresses the ejecta contribution because it is virtually free of the emission lines that arise mostly from the ejecta and dominate the broadband spectrum; the thick bright shell in the broadband image disappears in the 4–6 keV continuum image. The full-width-half-maximum radial extent of the arcs is seen to be only about $4-4.5''$, compared to the remnant radius of roughly $4'$. The inside half of the rim is thinner in the continuum image, consistent with the emergence of thermal line emission at the inside edge behind the forward shock.

There are also a number of bright “knots” in the hard X-ray continuum image, most notably near the eastern edge and in the southwest. These knots have previously been noted in the lower spatial resolution 4–6 keV image obtained by XMM-Newton (Decourchelle et al. 2001). Radio emitting knots in the eastern part of the remnant are not at the same location

as the X-ray continuum knots, but are slightly northward. Indeed, the radio knots appear to be better correlated with the Si emission, as noted by Decourchelle et al. (2001). The dense cloud of H gas discussed by Reynoso et al. (1999, their “eastern knot”) is offset by about 1' to the north of the eastern bright X-ray continuum knot.

2.2. Ejecta Distribution

The ejecta in Tycho’s SNR are visible only from their X-ray emission. The optical emission comes entirely from the forward shock, and the infrared emission is also associated with the forward shock (Douvion et al. 2001), while the radio emission is due to electrons accelerated at the shock rather than to ions. The general distribution of the ejecta is evident in the broadband X-ray image (Figure 1a), which is dominated by the Si line emission, and is seen even more clearly in the Si line image of Figure 1(b). Overall, the Si emission is distributed fairly uniformly on large scales, and is very clumpy in appearance, but not compact or knotty like the Si ejecta emission from Cas A (Hughes et al. 2000, Hwang et al. 2000).

To calibrate the observed Si line-to-continuum ratios in Figure 2b with the Si abundances, we used the ACIS detector response to compute the count rates expected from solar-abundance thermal models with various temperatures and ionization ages. We find that if the line-to-continuum ratio exceeds 3-4, the Si abundance must be enhanced above the solar value for temperatures above 0.7 keV, regardless of the ionization age. Lower values of the ratio could be consistent with enhanced abundances if the temperature is below 0.7 keV, depending on the ionization age. In the brightest Si clouds, the ratios are high enough that the element abundances must be well above solar, as expected. The finger-like projections that reach the forward shock in the west have lower values of the line-to-continuum ratio, but are shown to be associated with ejecta by the spectral analysis presented in the following section. The two large, bright, Si- and Fe- rich ejecta knots that bulge beyond the forward shock in the east were known prior to Chandra and XMM (Vancura et al. 1995, Hwang & Gotthelf 1997); it is now evident that Si ejecta reach the forward shock elsewhere in the remnant, though without distorting the remnant boundary. It is plausible that many of the Si clumps seen in the interior are similar to the finger-like features at the edges, but are seen face on.

Most of the Si emission is clumpy on angular scales greater than $\sim 5''$, but the continuum-subtracted Si line image (Figure 1b) shows low level emission throughout the remnant. This emission may be associated with a faint, smooth component of Si ejecta (see Wang & Chevalier 1999). To estimate the contribution of such a component, we smoothed the Si line image

with an adjustable beam containing at least 25 counts, subtracted the off-source background, and determined the lowest intensity level inside the remnant. Assuming that the faint emission is distributed uniformly over the remnant, we estimate that it makes up about 25% of the Si line photons. It is possible that this faint Si emission will appear clumpy when viewed at higher statistical significance, but clumps with a significant density enhancement should be readily visible since the X-ray luminosity scales as the square of the density. The surface brightness contrast of the faintest visually identified clumps in the image is a factor of two.

In comparison to the Si images, the Fe L and K line images appear to be somewhat less clumpy, but they are also much more sparse. Moreover, it is difficult to calibrate the Fe L image, as the numerous Fe L lines are blended with each other and with lines of Ne and O, so that the true continuum cannot be determined without detailed spectral modelling. Except for the prominent Fe-rich knot in the east, we cannot ascertain from the images alone whether Fe L emission is present at the forward shock. The brightest Fe K emission is certainly associated with ejecta, as the line-to-continuum ratio is generally high, and any ratio greater than 2 indicates enhanced abundances for any temperature or ionization age. The Fe K emission is radially interior to Fe L and Si, as has already been noted (Decourchelle et al. 2001, Hwang & Gotthelf 1997); as suggested by Decourchelle et al., this is likely to be the signature of the temperature and ionization structure behind the reverse shock. Detailed discussion of the ejecta spectra will be presented elsewhere.

3. Spectra of the Forward Shock

We study the spectrum of the forward shock along the outer rim in the southwest, northwest, and northeast, for the regions indicated in Figure 5. We avoid the eastern region, where the rim is not clearly defined, and where the remnant is interacting with dense H gas. The spectral regions are typically $5''$ wide, corresponding to 0.05 pc at a distance of 2.3 kpc. With the spectra from adjacent regions behind the rim, we sample angular distances up to about $10''$ behind the shock front. The size of the spectral regions and the counts in each spectrum are given in Table 2. With one exception, each spectrum has at least ~ 2000 counts. We bin the spectra to have at least 25 counts per pulse height channel, and fit the energy range from 0.5 keV up to 10 keV.

Using the tools in CIAOv2.2, we have customized the spectral calibration files for each spectrum. Since the gain and resolution vary with position on the detector, we use appropriately weighted detector response functions. Spectra were taken from a single CCD chip, S3, with the exception of region 5, which is mostly from S3, but includes a 15% contribution from S2. Although the spectral calibration of S2 is not as complete as for S3, the results

obtained for spectra taken from S2 are consistent with those from S3. We also combined the nearly featureless spectra from regions 1 and 2 in the southwest (on S2), and regions 4 and 5 in the northwest (on S2 and S3) to improve the signal-to-noise-ratio. Background spectra are taken from source-free regions on the same CCD chip (or a weighted combination from both chips, if appropriate). We fitted the spectra with both nonthermal and thermal models, as described in the following sections.

It has recently come to light that ACIS suffers from a time-dependent absorption due to the build-up of contaminants on the detector (see <http://cxc.harvard.edu>). The effects of this absorption increase with time and can be included in either the response function or the spectral model. For our observation, taken only 424 days after launch, the effect of this absorption on the fitted spectra is relatively small. When we include its effect in the spectral model, we find that the interstellar absorbing column density is the only parameter that is significantly affected, being reduced by about 5×10^{20} cm $^{-2}$ from the values in Table 4.

3.1. Models

For fitting thermal models, we primarily use single temperature, single ionization age, nonequilibrium ionization models (XSPEC v11.0, Borkowski, Lyerly, & Reynolds 2001). The ionization age $n_e t$ is defined as the product of electron density and time since shock-heating, and parameterizes the progress toward ionization equilibrium of gas that is suddenly heated to a high temperature. Because we take very narrow regions behind the shock front, this simple model is an excellent approximation for the spectra at the rim. In the cases where the fitted ionization age is very low because of the absence of line emission, we find that a simple NEI model is essentially indistinguishable from models that approximate the emission behind a segment of a planar shock wave using a range of ionization ages (p_{shock}), or from a simple bremsstrahlung continuum. Detailed comparisons are shown in Table 3 for such a case—the featureless spectrum from the northwest rim segments 4 and 5.

For fitting nonthermal models, we favor the synchrotron radiation cutoff model (srcut ; see Reynolds & Keohane 1999, Dyer et al. 2001) over simple power-law models. The srcut model folds the single particle synchrotron emissivity with a power-law electron energy distribution having an exponential cutoff. It is the most appropriate readily-available model for describing the synchrotron spectrum with the fewest assumptions. It takes as parameters the radio spectral index, the frequency at which the spectrum rolls off (to a factor of 6 below the extrapolation of the radio spectrum, Reynolds 1998), and the radio flux at 1 GHz as the normalization. Reynolds & Keohane use this model with the spatially integrated X-ray spectrum of Tycho’s SNR and the observed radio brightness and spectral index to determine

the energy at which the photon spectrum must roll off if the model is not to exceed the observed X-ray spectrum. The electron energy is then determined from the rolloff frequency by taking the magnetic field to be a fiducial value of $10 \mu\text{G}$. Reynolds & Keohane estimate the rolloff frequency to be $8.8 \times 10^{16} \text{ Hz}$ on average (corresponding to an energy of 0.4 keV), to set the upper limit on the cutoff energy of the electron spectrum at 40 TeV.

In our use of the *srcut* model, we take the appropriate slope of the radio spectrum for each region of the remnant from Katz-Stone et al. (2000). The normalization of the model is taken to be the radio flux at 1 GHz, and the rolloff frequency is freely fitted. To obtain the radio flux for each spectral region, we use the 1.36 GHz (22 cm) image of Dickel et al. (1991). This 1983 image is of lower angular resolution than the Chandra image, but all the spectral regions we use are much larger than the radio beam size. We first scale the radio image to match the Chandra image, and then extract the radio fluxes from the same spatial regions used for the X-ray spectral analysis. To convert the flux at 1.36 GHz to the value at 1 GHz, we simply took the product of the fraction of the total 1.36 GHz flux in each spectral region with the total 1 GHz flux of 56 Jy (Green 2001). An indication of the uncertainty in the radio flux is given by the difference between the 1.36 GHz flux in our image and that determined by extrapolating a 1 GHz flux of 56 Jy using the average radio spectral index of 0.50 (Katz-Stone et al. 2000); this difference is about 15%.

Comparisons of thermal and nonthermal model fits for the northwest rim are also shown in Table 3. The *srcut* model gives a somewhat better fit than a simple power-law. Also shown is a hybrid containing both thermal and nonthermal components, to be discussed in more detail in the following section. The northwest region of the remnant is notable for having the highest value measured for the radio spectral index, at 0.72 ± 0.14 (Katz-Stone et al. 2000), but it is evident from our spectral fits that the higher-than average spectral index determined in the radio is not compatible with the radio flux together with the X-ray spectrum in the context of the *srcut* model. Even allowing for $\sim 15\%$ uncertainty in the radio flux normalization, an acceptable fit requires the radio spectral index to be below the low end of its error range, at a value closer to the overall average value found for the remnant. This does not seem implausible, given the difficulties inherent in measuring the radio spectral index.

3.2. Results for Rims

For the complete set of spectra at and behind the rim, we present the results for the thermal NEI models in Table 4 and Figure 6. The spectra in the northwest and southwest sections are pristine and show very little evidence for any line emission. The other rim

spectra do show weak line emission, especially from Si and S, but generally not from Fe L; most of the spectra taken from behind the rim also show the emergence of line emission. We use a single NEI component with solar abundances to represent the forward shock, unless the poor quality of the fit warrants the addition of a second component. Since line emission is generally responsible for the poorer fits with single component models, this second component represents ejecta (we choose a criterion of $\chi^2/dof \gtrsim 1.3$). The forward shock temperatures obtained are very similar around the entire rim, at about 2 keV, and the ionization age is uniformly low, with upper limits in the range of a few $10^8 \text{ cm}^{-3} \text{ s}$.

For cases like region 3 in the west, the line emission seen in the spectrum is clearly from Si and S ejecta, as is corroborated by the Si equivalent width image (Figure 2b). The line emission can be modelled with a NEI component containing only the intermediate mass elements Si and S in their solar abundance ratios (with the exception of the region behind rim 3 which requires enhanced S), and generally without significant Fe or Ni. This may be justified by the observation that the Si ejecta are, on average, more abundant at large radii than Fe ejecta (see Hwang & Gotthelf 1997). The fits are not sensitive to the temperature assumed for the ejecta, as a large range of temperatures will give satisfactory results if the ionization age is adjusted. We therefore warn that the ionization ages determined for the ejecta in Tables 4-6 should not be taken too seriously. We used an ejecta temperature of 0.9 keV, following the results for the globally averaged spectra (Hwang & Gotthelf 1997). In a few instances, the fits are substantially improved with the addition of Fe and Ni in the ejecta, generally with abundances well below the solar ratio relative to Si and S (see Table 4). In other cases, such as regions 6 or 7, the line emission may not necessarily be from ejecta, as lines of O, Ne, and Fe are present in addition to those of Si and S. This tends to be true of the regions in the north or northwest, which are also distinguished by the presence of optical emission and by distortions of the remnant boundary.

The fitted ionization ages behind the northern rim are higher than those at the rim—a result one would expect since the interstellar gas behind the rim was shocked at an earlier time. For the northwest and southwest regions (1, 2, 4, and 5), however, the fitted ionization ages behind the rim remain low, with upper limits consistent with those at the rim itself. This much smaller (i.e., undetectable in our data) change in the ionization age is qualitatively consistent with a lower density for the interstellar gas in the northwest and southwest than in the north. In turn, this is broadly consistent with the interaction of the remnant with denser gas to the north and east that is indicated by the radio observations and the presence of optical emission. The typical radio shock velocity is about 3000-4000 km/s all along the western edge of the remnant. For a velocity of 3500 km/s, a distance of 5" behind the shock would imply an increase in the ionization age n_{et} by about $6 \times 10^8 \text{ cm}^{-3} \text{ s}$ for an ambient density of 0.3 cm^{-3} for Tycho's SNR (e.g. Seward et al. 1983). Upper limits for the

ionization age of $2 - 3 \times 10^8 \text{ cm}^{-3} \text{ s}$ at and behind the rim in the northwest and southwest (regions 1, 2, 4, and 5) require a lower density closer to about $0.1\text{-}0.15 \text{ cm}^{-3}$; the higher ionization age of a few 10^9 cm^{-3} measured in the north and northeast (regions 6, 7, and NE) would suggest higher ambient densities above 1 cm^{-3} . For a higher shock velocity, the expected change in ionization age would be proportionally lower.

In our fits, higher ionization ages are also generally accompanied by higher fitted column densities that are associated with the need to absorb the He-like O lines predicted by the models. These are inconsistent, however, with the column density of $4.5 \times 10^{21} \text{ cm}^{-2}$ determined in the radio towards Tycho's SNR (Albinson et al. 1986), and with the fitted column densities for the adjacent regions on the rim. This discrepancy most likely indicates spectral complexity that is not well-represented by a single temperature and ionization age for all the elements. We were not able to resolve it with any simple spectral models.

A third set of spectra taken directly behind the two sets already discussed for rim segments 1, 2, 4, and 5 do finally show the emergence of strong emission lines of Si and S associated with the ejecta. The ionization age limits for the forward shocked component continue to be low at a few $10^8 \text{ cm}^{-3} \text{ s}$ for all except region 5. The best two-component fit for region 5 shows a large increase in the ionization age associated with the forward shock, but it also shows a large increase in the column density, suggesting that the simple two-component model is not fully adequate.

Results of the nonthermal fits are given in Table 5 for the prominent major sections of the rim. The quality of the fits is generally comparable to, or perhaps slightly worse than the thermal model fits. The ejecta are included in the model for the NE filament, following the preceding discussion for the thermal fits. The radio flux has been fixed for the fits, but allowing the radio normalization to vary between 15% limits typically affects the fitted spectral index or rolloff frequency by 20-30%. The spectrum of the northeast rim is entirely consistent with the radio spectral index, giving a rolloff frequency near $5 \times 10^{16} \text{ Hz}$ that is slightly lower than that estimated by Reynolds & Keohane (1999) for the spatially integrated spectrum of Tycho's SNR. For the southwest, the fitted radio spectral index is acceptable, but an improved fit can be obtained with a slightly higher value that is closer to the overall average, and entirely consistent with the uncertainties in the radio measurement. Again, the rolloff frequency is then near $5 \times 10^{16} \text{ Hz}$. The situation in the northwest has already been discussed: the value of the radio spectral index favored by the X-ray spectral fits is marginally incompatible with the radio measurement, and the fitted rolloff frequency is possibly slightly higher than in the other sections of the rim that we examined.

The fitted values of the rolloff frequency ν in Table 5 can be used to deduce the maximum electron energy E , given the strength of the magnetic field B , using Eq. (2) of Reynolds &

Keohane (1999):

$$\nu(\text{Hz}) = 0.5 \times 10^{16} \text{Hz} \left(\frac{10 \mu\text{G}}{B} \right) \left(\frac{E}{10 \text{TeV}} \right)^2.$$

Reynolds & Ellison (1992) estimate the magnetic field strength in Tycho’s SNR to be $10^{-4} - 10^{-2}$ G. Taking the rolloff frequencies from Table 5 and the lower end of the values for the magnetic field, the maximum electron energies are 8-14 TeV; using the upper end of the magnetic field values, the maximum electron energies are 10 times lower, at ~ 1 TeV.

The continuum may actually be a mixture of thermal and nonthermal emission, but it is difficult to disentangle these contributions from these spectra alone. The spectra may be fitted with such a hybrid continuum model, but the fits are not substantially improved. In the example given in Table 3, the best fit is very strongly dominated by the thermal component and the determination of the temperature is therefore not adversely affected. In other cases, there are two statistically comparable local minima in the parameter space—one where the nonthermal component dominates the flux, and the other where the thermal component dominates the flux. When the thermal component dominates the flux, the temperature inferred for the thermal component is not very different from the case with no nonthermal contamination. When the nonthermal component dominates the flux, it is not surprising that the temperature of the thermal component is more poorly constrained, with errors that can be as much as two times larger. Good fits may indeed sometimes be obtained with a hybrid model that is dominated by the nonthermal component, but in these cases, the thermal component takes on a low temperature and high ionization age in order to fit the weak line emission from ejecta. From our exploration of the spectra, we conclude that it is not likely for the temperature of the thermal component to be substantially higher than deduced using the purely thermal models.

3.3. Results for Hard Continuum Knots

We also examined the spectra of two prominent knotty features present to the east and the west in the hard X-ray continuum image. The spectra of both knots clearly show emission lines, and the western knot (CKW) is strongly contaminated by the presence of Si and S ejecta. To fit the spectra, we used two-component NEI models to represent solar abundance forward shocked gas and reverse shocked Si and S ejecta, as discussed in the previous section and shown in Table 6. The fitted ionization age for the forward shock component in CKW is significantly higher than for the rims, at a few $10^9 \text{ cm}^{-3} \text{ s}$, while the eastern knot (CKE) appears to favor a low ionization age.

The eastern feature CKE is near, but not at, the eastern boundary of the remnant, and

the western feature CKW is well inside the western boundary. It is possible that these are similar to the rim features that are seen along the west and south, except that by projection they appear in the interior of the remnant. Their higher surface brightness in the hard continuum image is qualitatively consistent with their higher fitted temperatures (~ 3 keV, compared to 2 keV), but their true nature remains elusive. The CKW feature has a higher fitted ionization age than the rest of the rim, and while this can generally be explained by a higher density, the ambient density is known to be higher in the east than it is in the west. One would therefore expect the opposite case of a higher ionization age for CKE than for CKW. If nonthermal emission were dominant, features corresponding to the knots might be expected in the radio images, but none are seen.

4. Discussion

4.1. Electron Temperatures

We combined the X-ray spectral results with the radio and X-ray expansion velocities to estimate the ratio of electron to ion temperatures behind the forward shock in Tycho’s SNR. The temperature attained by particles as they pass behind the shock depends on their mass according to the shock jump conditions as $kT \sim \frac{3}{16}mv_s^2$, where m is the particle mass and v_s the shock velocity. The different particle species will exchange energy through Coulomb collisions and eventually attain a single equilibrium temperature, but it has been proposed that this equilibration may be effected much faster by collective plasma interactions (Cargill & Papadopoulos 1988). The efficiency of these collisionless heating processes appears to decrease in inverse proportion to the Mach number of the forward shock, however, so that they may be less important for the fast shocks associated with young supernova remnants (Laming et al. 1996, Ghavamian et al. 2001). The electrons behind the slower shocks in the Cygnus Loop, for example, have virtually equilibrated with the ions, in contrast to those behind the faster shocks of younger remnants such as SN 1006.

We plot in Figure 8 the equilibrium temperatures for Tycho’s SNR corresponding to the radio expansion parameters determined as a function of azimuthal angle (defined counterclockwise from north) by Reynoso et al. (1997). We use their Table 2 and Figure 5, and a distance of 2.3 kpc, to compute the velocities, and take the mean molecular weight per particle to be μm_p , with $\mu = 0.6$ for solar abundance gas and m_p being the proton mass. The rather large fluctuations for angles greater than 180° are attributed by Reynoso et al. (1997) to uncertainties in determining the remnant radius. Also shown in the figure are the equilibrium temperatures corresponding to the average radio expansion velocity, and the average X-ray expansion velocity given by Hughes (2000). It is not yet clear which of the

radio or X-ray expansion values should be used, though the radio measurement is made with higher angular resolution data. Also, if the ejecta presently located near the forward shock have high velocities, they might bias the X-ray expansion measurement, as suggested by Wang & Chevalier (2001). This question will hopefully be better resolved with a new study of the X-ray proper motion using higher spatial resolution data.

The data points in the Figure give the temperatures determined along the rim from our fits, assuming that the X-ray emission is thermal (Table 4); the appropriate azimuthal angle is determined with reference to the center adopted by Reynoso et al. (1997). The electron temperatures we measure are clearly much lower than the mean temperatures expected for shock velocities determined from the radio expansion, with electron to mean temperature ratios of 0.10–0.20. If we scale the mean temperature by the ratio of the average X-ray velocity to the average radio velocity, it increases by a factor of two, and the electron to mean temperature ratios decrease accordingly. Although electron-ion temperature equilibration is not attained, the electron temperatures are higher than would be expected from Coulomb heating alone. Ionization ages as low as $10^8 \text{ cm}^{-3} \text{ s}$ allow for negligible electron heating mediated by Coulomb collisions. The measured electron temperature is thus essentially the electron temperature attained immediately after passage through the shock front, and represents extra heating in addition to Coulomb heating.

A low degree of electron-ion equilibration is consistent with results from the optical spectra for the brightest knot in Tycho’s SNR (knot *g*), where the electron to proton temperature ratio is $\lesssim 0.1$ (Ghavamian et al. 2001). The degree of electron-ion equilibration has also been determined to be low in SN 1006, with the electron-to-proton temperature ratio $\lesssim 0.05$ using UV spectra (Laming et al. 1996). In SN 1987A, the temperatures measured from Chandra X-ray spectra are also lower than would be expected for equilibrium based on the observed radio and X-ray expansion of the remnant (Michael et al. 2002). The implied ratio of electron and mean particle temperatures is about 0.1, giving an electron to proton temperature ratio of about 0.07 (with $\mu = 7$ for the N-enriched circumstellar material surrounding SN 1987A). The X-ray line profiles (observed with the high spectral resolution High Energy Transmission Gratings on Chandra) are also consistent with thermal broadening due to high ion temperatures behind the shock. All these results are summarized in Figure 9. For comparison, the model of Cargill & Papadopoulos (1988) for rapid electron heating can accommodate electron-to-ion temperature ratios of about 0.20.

In contrast to these cases, the measured electron temperature behind the forward shock in the Small Magellanic Cloud remnant E0102-72 is lower than would be expected for the X-ray determined shock velocity, even with Coulomb heating alone. In this case, the low temperature is interpreted as evidence for highly efficient, nonlinear acceleration of particles

behind the shock front (Hughes, Rakowski, & Decourchelle 2000). There is independent evidence that nonlinear acceleration of electrons may be occurring in Tycho’s SNR, in that the observed curvature of the radio electron synchrotron spectrum is predicted by such models (Reynolds & Ellison 1992). The brightness of the radio emission at the rim also requires the fresh acceleration of particles at the shock (Dickel et al. 1991), and this process may extend to sufficiently high energies to affect the X-ray emission. The temperatures expected behind shocks where efficient particle acceleration takes place are lower, making the ratio of measured electron temperature to mean temperature ratios higher than otherwise.

For the bright continuum knot in the east, the observed temperature is actually consistent with temperature equilibration behind a shock at the radio velocity. The radio velocity of the rim may not be applicable there, however, as the knot is interior to the rim and is probably only projected there. This knot is also very near the position of the optical knot g , for which Ghavamian et al. (2001) determine that the electron temperature should be no higher than 0.8 keV, at 0.1 times the proton temperature. However, there is a 10" nominal offset between the X-ray and optical (Kamper & van den Bergh 1978) position, whereas the nominal X-ray coordinate uncertainty should be well under 3" (Chandra Proposer’s Observatory Guide); the optical measurements are probably not applicable to the continuum knot either. One of the radio velocity points applicable to rim segment 4 is also consistent with the measured X-ray temperature, but this point represents a sharp excursion well below the average.

The foregoing discussion is based on the assumption that the emission is thermal, but it has been seen that nonthermal and thermal models are about equally successful in individually describing the featureless rim spectra. In section 3.2, we argued that the spectra indicate that the temperatures should not be much higher than determined from the thermal fits alone, even in the presence of nonthermal emission. In the next section, we present evidence that an additional nonthermal component is indeed likely to be present.

4.2. Nonthermal and Thermal Emission Components

Hard X-ray emission has been unmistakably detected from Tycho’s SNR, at energies up to 25 keV with HEAO-1 (Pravdo et al. & Smith 1979), 20 keV with Ginga (Fink et al. 1994); and 30 keV with RXTE (Petre et al. 1999). Several models have been proposed to explain the hard X-ray continuum in Tycho’s SNR as synchrotron radiation from electrons accelerated at the shock (Heavens 1984, Ammosov et al. 1994). Given that the temperatures (in thermal models) at the forward shock in Tycho’s SNR are only about 2 keV, the X-ray emission at higher energies may well have a nonthermal origin, as has been suggested in the

literature.

We estimate an upper limit to the nonthermal X-ray luminosity from Tycho’s SNR in the Chandra energy band by attributing *all* the flux between 4-6 keV to a nonthermal component. This is clearly an overestimate because there is a hot thermal component associated with the Fe K line emission (Hwang et al. 1998). We first obtained the total source counts between 4-6 keV by estimating and subtracting the background counts from the continuum image and multiplying by a rough geometrical correction factor of 1.15 for the portion of the remnant that was not imaged. We then took the 0.5-10 keV source luminosity of the nonthermal model for the northwest rim and scaled it up by the ratio of 4-6 keV counts in the total image to those in the rim segment, to estimate the nonthermal luminosity for the entire remnant. This maximum luminosity is about 2×10^{35} ergs/s, but could be reduced by a factor of a few if we use only the bright X-ray continuum regions in the rim and the knots in our estimate. We have not accounted for the variation in radio spectral index for different parts of the remnant, but if we use the spectrum fitted to the southwest rim, which has a much flatter radio slope, the estimated luminosity is essentially unchanged.

One can also estimate this nonthermal luminosity for Tycho’s SNR by extrapolating the flat component in the Ginga or RXTE X-ray spectra down to energies in the Chandra band. Extrapolating the power-law model given by Fink et al. (1994) for the Ginga data, we estimate a 0.5-10 keV nonthermal luminosity of about 1.5×10^{35} erg/s. Aharonian et al. (2001) fitted the RXTE spectrum with a model that includes an exponential cutoff, although they inferred a steeper radio slope than is actually observed overall, and obtained a higher turnover energy of 1.6 keV ($\nu = 3.8 \times 10^{17}$ Hz). The 0.5-10 keV luminosity implied by their model is 1×10^{35} ergs/s. Both estimates are a substantial fraction of the maximum possible luminosity from our estimate above, indicating that perhaps half of the hard 4-6 keV X-ray emission in Tycho’s SNR is nonthermal. The nonthermal luminosity estimated from these hard X-rays is slightly higher than that of SN 1006 in the same energy range (Dyer et al. 2001).

The nonthermal X-ray emission should also be accompanied by γ -ray emission, since the energetic electrons that emit the X-ray synchrotron radiation will also upscatter cosmic background photons. The γ -ray upper limits for Tycho’s SNR have become tighter in recent years (Aharonian et al. 2001), at levels that are a few to several times lower than the detections for SN 1006 (Tanimori et al. 1998). This may be understandable from a consideration of the densities and magnetic fields in these remnants. The extrapolation of the radio spectrum to the X-ray range gives maximum electron energies comparable to those determined for SN 1006 (Reynolds & Keohane 1999), if equal magnetic field strengths of $10 \mu\text{G}$ are assumed. A magnetic field of 10^{-4} to 10^{-2} G in Tycho’s SNR from Reynolds &

Ellison (1992) is higher than the $9 \mu\text{G}$ in SN 1006 (Dyer et al. 2001). A higher magnetic field qualitatively accounts not only for the more severe synchrotron energy losses of the electrons in Tycho’s SNR, but also its higher radio surface brightness. The maximum electron energies will be lower in proportion to $B^{-1/2}$; on the basis of our spectral fits, the maximum electron energies would appear to be between 1-15 TeV, depending on the exact value of the magnetic field. The much lower density environment of SN 1006 (e.g., see Kirshner et al. 1987) would also allow particle acceleration to proceed to higher energies in the first place (Baring et al. 1999).

4.3. Mixing of Ejecta

The presence of ejecta at the forward shock requires a significant amount of mixing either during or after the explosion. Various high resolution hydrodynamical studies (Dwarkadas 2000, Wang & Chevalier 2001) show that the ejecta cannot penetrate beyond about half the interaction region through Rayleigh-Taylor instabilities alone, though early Richtmyer-Meshkov instabilities might enhance the effectiveness of the Rayleigh-Taylor instabilities (Kane et al. 1999). Clumps in the ejecta (Hamilton 1985) or in the interstellar medium (Jun, Jones & Norman 1996) would, however, allow the ejecta to penetrate to large radii. Ejecta might also penetrate the forward shock in the presence of enhanced turbulence generated as the reverse shock propagates into low density bubbles of Fe, formed as the heat release from the radioactive decay of clumps of Ni ejecta allows them to expand (Blondin et al. 2001). Yet another possibility is that the ejecta can affect the forward shock when the interaction region for the shock is very thin, as could be the case with nonlinear particle acceleration behind the forward shock—a situation that might reasonably be expected to occur in young remnants (Blondin & Ellison 2001), including Tycho’s SNR in particular (Reynolds & Ellison 1992). The action of the Rayleigh-Taylor instabilities out to the forward shock is further supported by the radial orientation of the magnetic field (Dickel et al. 1991), which is observed all the way to the rim of the remnant.

One might expect that if the ejecta do penetrate the forward shock, the boundary of the outer shock would be distorted, whereas the western boundary of Tycho’s SNR is smooth and circular. This might still be possible, however, if the mixing occurred early enough for the protruberances to have subsided. In their simulations, Wang & Chevalier (2001) found that it was actually difficult to deform the forward shock unless the ejecta density contrast was very high.

The qualitative appearance of the Si ejecta in Tycho’s SNR is quite different from that of the core-collapse remnant Cas A, which has also been beautifully imaged by Chandra

(Hughes et al. 2000, Hwang et al. 2000). While the Si is clumpy in Tycho, it is compact and knotty in Cas A. Despite the fact that Tycho is located at a smaller distance, the angular scale of its Si features is larger than those seen in Cas A. Differences are also seen in the 4-6 keV continuum images. In Tycho’s SNR, the ejecta shell has virtually disappeared in this image, but in Cas A, the ejecta are still clearly visible. The emission associated with the ejecta is thus seen to be relatively more important at these energies in Cas A than in Tycho’s SNR. Indeed, the hard X-ray emission in Cas A has been proposed to be primarily bremsstrahlung emission from electrons that have been accelerated in the ejecta (Laming 2001ab, Bleeker et al. 2001).

The appearance of the forward shock in these two remnants is also strikingly different. Tycho’s outer rim is distorted because of its interaction in the east, but the outline of the rim is otherwise generally smooth and continuous. By contrast, the outer rim of Cas A is broken up on small scales and shows tightly curved fragments (Gotthelf et al. 2001). If some of this emission is nonthermal, this may reflect differences seen in their radio emission, as Tycho has a sharp radio rim suggesting efficient first order Fermi acceleration, whereas Cas A has no distinct radio rim and is a better candidate for second order Fermi acceleration mediated by turbulence (e.g., Dickel et al. 1991). SN 1006, another Type Ia remnant, shows the same smooth outer rim seen in Tycho’s SNR, and the same highly clumpy ejecta (in this case O ejecta; K. Long, private communication), but this is still much too small a sample for these differences to be more than suggestive.

5. Summary

The Chandra observatory allows the imaging and spectral study of the forward shock in Tycho’s SNR. The Si ejecta are highly clumpy and have propagated to the forward shock in several locations. The spectra at the rim show slight, but varying amounts of line emission, with continua that are well described by either thermal or nonthermal models. Spectra behind the shock show stronger line emission consistent with this gas having been shocked at earlier times. The limits on the change in ionization age behind the rim give some indication of variations in density around the remnant. Taking the electron temperature from thermal models, combined with the results of radio and X-ray expansion studies, the electron to mean temperature ratios behind the shock are $\lesssim 0.1 - 0.2$, indicating a modest amount of electron heating, but not full temperature equilibration. A consideration of the hard X-ray emission suggests, however, that an additional nonthermal component must be present. Even in the presence of such a nonthermal component, the electron temperatures do not seem likely to significantly exceed the values we measure assuming purely thermal models. Ideally, it is

desirable to have energy coverage that continues above 10 keV to disentangle the nonthermal and thermal contributions to the spectrum, but such observations will not be possible in the near future.

For future work, a useful first step would be imaging the distribution of the high energy X-ray flux above 8 keV, as would be possible with XMM-Newton. To the extent that the hard X-rays are distributed like the 4-6 keV X-rays at the rim of the remnant (as seems likely), this would be consistent with their origin from electrons accelerated to high energies. It would also be beneficial to model as wide a bandwidth spectrum as possible, and to carry out a detailed study of the radio and X-ray correlations, as well as to consider the effects of nonlinear particle acceleration.

We are grateful to John Dickel for generously providing his flux-normalized 22 cm radio image, Ramesh Narayan for an inspiring conversation, and Andrew Szymkowiak for several helpful scientific discussions. We also thank our anonymous referee for a very careful review of the manuscript.

REFERENCES

Aharonian, F., et al. 2001, *A&A*, 373, 292

Albinson, J. S., Tuffs, R. J., Swinbank, E., & Gull, S. F. 1986, *MNRAS*, 219, 427

Ammosov, A. E., Ksenofontov, L. T., Nikolaev, V. S., & Petukhov, S. I. 1994, *Astr. Lett.*, 20, 157

Baring, M. G., Ellison, D. C., Reynolds, S. P., Grenier, I. A., & Goret, P. 1999, *ApJ*, 513, 311

Bleeker, J. A. M., Willingale, R., van der Heyden, K., Dennerl, K., Kaastra, J. S., Aschenbach, B., & Vink, J. 2001, *A&A*, 365, L225

Blondin, J. M., Borkowski, K. J., & Reynolds, S. P. 2001, *ApJ*, 557, 782

Blondin, J. M., & Ellison, D. C. 2001, *ApJ*, 560, 244

Borkowski, K. J., Lyerly, W. J., & Reynolds, S. P. 2001, *ApJ*, 548, 820

Cargill, P. J., & Papadopoulos, K. 1988, *ApJ*, 329, L29

Chevalier, R. A., Kirshner, R. P., & Raymond, J. C. 1980, *ApJ*, 235, 186

Chevalier, R. A., & Raymond, J. C. 1978, *ApJ*, 225, L27

Decourchelle, A., Ellison, D. C., & Ballet, J. 2000, *ApJ*, 543, L57

Decourchelle, A., Sauvageot, J. L., Audard, M., Aschenbach, B., Sembay, S., Rothenflug, R., Ballet, J., Stadlbauer, T., & West, R. G. 2001, *A&A*, 365, L218

Dickel, J. R., Sault, R., Arendt, R. G., Korista, K. T., & Matsui, Y. 1988, *ApJ*, 330, 254

Dickel, J. R., van Breugel, W. J. M., & Strom, R. G. 1991, *AJ*, 101, 2151

Douvion, T., Lagage, P. O., Cesarsky, C. J., & Dwek, E. 2001, *A&A*, 373, 281

Dwarkadas, V. V. 2000, *ApJ*, 541, 418

Dyer, K. K., Reynolds, S. P., Borkowski, K. J., Allen, G. E., & Petre, R. 2001, *ApJ*, 551, 439

Fink, H. H., Asaoka, I., Brinkmann, W., Kawai, N., & Koyama, K. 1994, *A&A*, 283, 635

Ghavamian, P., Raymond, J., Smith, R. C., & Hartigan, P. 2001, *ApJ*, 547, 995

Gotthelf, E. V., Koralesky, B., Rudnick, L., Jones, T. W., Hwang, U., & Petre, R. 2000, *ApJ*, 552, L39

Green D.A., 2001, ‘A Catalogue of Galactic Supernova Remnants (2001 December version)’, Mullard Radio Astronomy Observatory, Cavendish Laboratory, Cambridge, United Kingdom (available on the World-Wide-Web at “<http://www.mrao.cam.ac.uk/surveys/snrs/>”)

Hamilton, A. J. S. 1985, *ApJ*, 291, 523

Heavens, A. F. 1984, *MNRAS*, 211, 195

Hughes, J. P. 1999, *ApJ*, 528, 298

Hughes, J. P. 2000, *ApJ*, 545, L53

Hughes, J. P., Rakowski, C. E., Burrows, D. N., & Slane, P. O. 2000, *ApJL*, 528, L109

Hughes, J. P., Rakowski, C. E., & Decourchelle, A. 2000, *ApJ*, 543, L61

Hwang, U., & Gotthelf, E. V. 1997, *ApJ*, 475, 665

Hwang, U., Holt, S. S., & Petre, R. 2000, *ApJ*, 537, L119

Hwang, U., Hughes, J. P., & Petre, R. 1998, *ApJ*, 497, 833

Jun, B.-I., Jones, T. W., & Norman, M. L. 1996, *ApJ*, 468, L59

Kamper, K. W., & van den Bergh, S. 1978, *ApJ*, 224, 851

Kane, J., Drake, R. P., & Remington, B. A. 1999, *ApJ*, 511, 335

Katz-Stone, D. M., Kassim, N. E., Lazio, T. J. W., & O’Donnell, R. 2000, *ApJ*, 529, 453

Kirshner, R. P., Winkler, P. F., & Chevalier, R. A. 1987, *ApJ*, 315, L135

Koralesky, B., Rudnick, L., Gotthelf, E. V., & Keohane, J. W. 1998, 505, L27

Koyama, K., Petre, R., Gotthelf, E. V., Hwang, U., Matsura, M., Ozaki, M., & Holt, S. S. 1995, *Nature*, 378, 255

Laming, J. M. 2001a, *ApJ*, 546, 1149

Laming, J. M. 2001b, *ApJ*, 563, 828

Laming, J. M., Raymond, J. C., McLaughlin, B. M., & Blair, W. P. 1996, *ApJ*, 472, 267

Michael, E., et al. 2002, *ApJ*, 574, 166

Petre, R., Allen, G. E., & Hwang, U. 1999, *Astr. Nach.* 320, 199

Pravdo, S. H., & Smith, B. W. 1979, *ApJ*, 234, L195

Reid, P. B., Becker, R. H., & Long, K. S. 1982, *ApJ*, 261, 485

Reynolds, S. P. 1998, *ApJ*, 493, 375

Reynolds, S. P., & Ellison, D. C. 1992, *ApJ*, 399, 75

Reynolds, S. P., & Keohane, J. W. 1999, *ApJ*, 525, 368

Reynoso, E. M., Moffett, D. A., Goss, W. M., Dubner, G. M., Dickel, J. R., Reynolds, S. P., & Giancani, E. B. 1997, *ApJ*, 491, 816

Reynoso, E. M., Velázquez, P. F., Dubner, G. M., & Goss, W. M. 1999, *AJ*, 117, 1827

Seward, F., Gorenstein, P., & Tucker, W. 1983, *ApJ*, 266, 287

Smith, R. C., Kirshner, R. P., Blair, W. P., & Winkler, P. F. 1991, *ApJ*, 375, 652

Strom, R. G., Goss, W. M., & Shaver, P. A. 1982, *MNRAS*, 200, 473

Tanimori, T., et al. 1998, *ApJ*, 497, L27

Vancura, O., Gorenstein, P., & Hughes, J. P. 1995, 441, 680

Vink, J., Bloemen, H., Kaastra, J. S., & Bleeker, J. A. M. 1998, *A&A*, 339, 201

Wang, C.-Y. & Chevalier, R. A. 2001, *ApJ*, 549, 1119

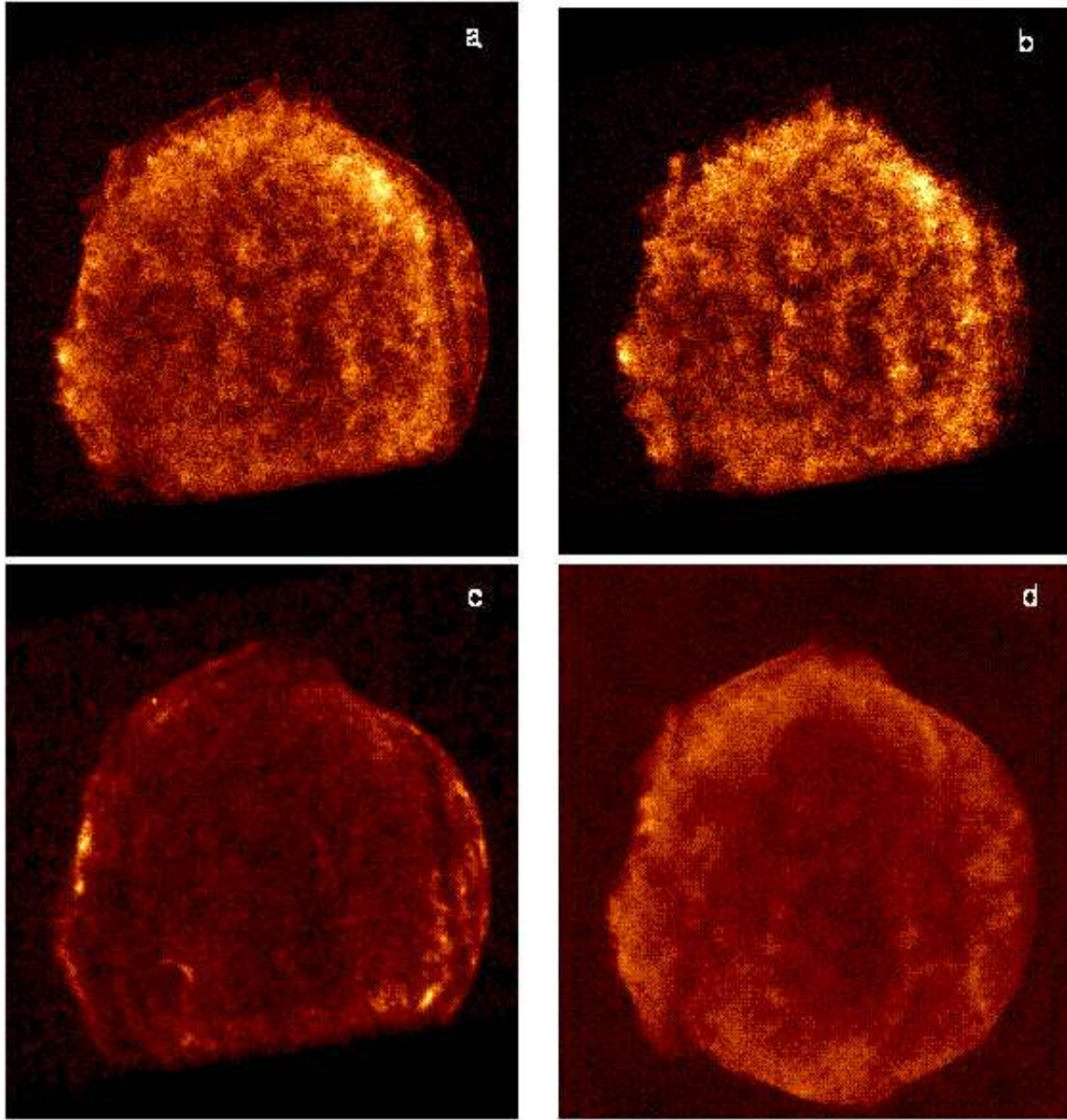


Fig. 1.— (a) Unsmoothed broadband Chandra ACIS image of Tycho's SNR. Most of the remnant is imaged on S3, but the western portion falls on S2 (the chip gap is visible), and the southernmost portion is not imaged. (b) Unsmoothed image of the Si emission lines near 1.86 keV with the underlying continuum subtracted. (c) Smoothed image of the hard continuum region at energies between 4-6 keV. (d) Radio image at 22 cm (1.36 GHz, epoch 1983; courtesy of John Dickel), convolved with a beam of width $1.45'' \times 1.38''$. All images have a square-root intensity scaling, except the radio image, which has a linear scaling. North is up and east to the left. The remnant is roughly 8' across.

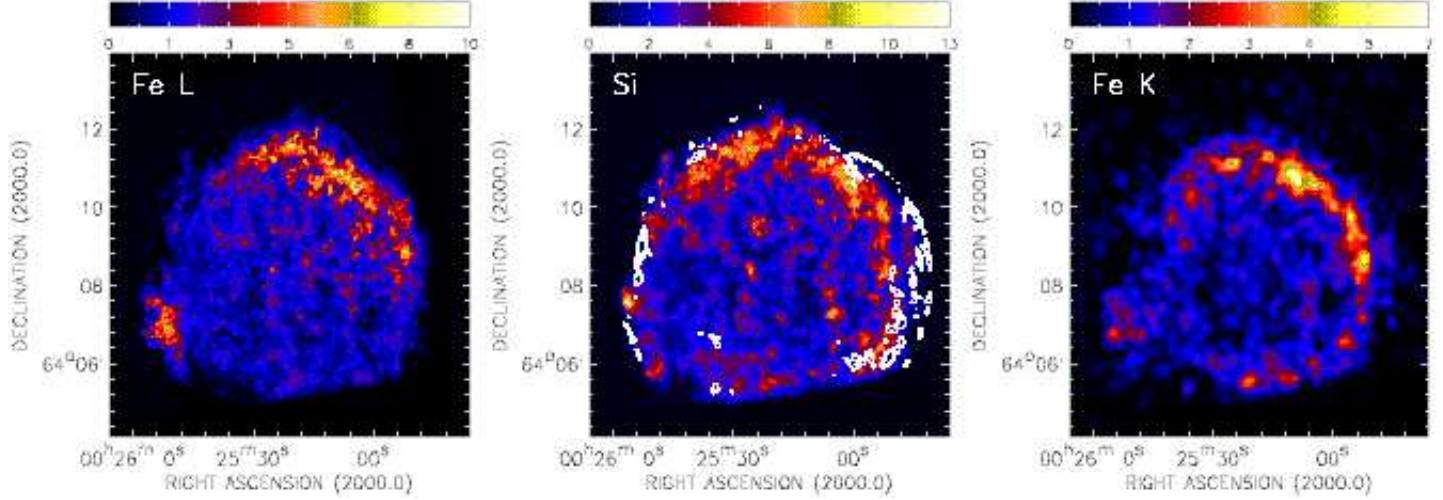


Fig. 2.— Equivalent width (continuum-subtracted, line-to-continuum ratio) image of (a, left) Fe L emission ($n=2$ transitions near 1 keV) (b, middle) Si emission (transitions of He- and H-like ions near 1.86 keV and 2.006 keV), with low-level (10 and 20% maximum) contours of the smoothed continuum emission overlaid (c, right) Fe K emission ($n=1$ transitions near 6.5 keV).

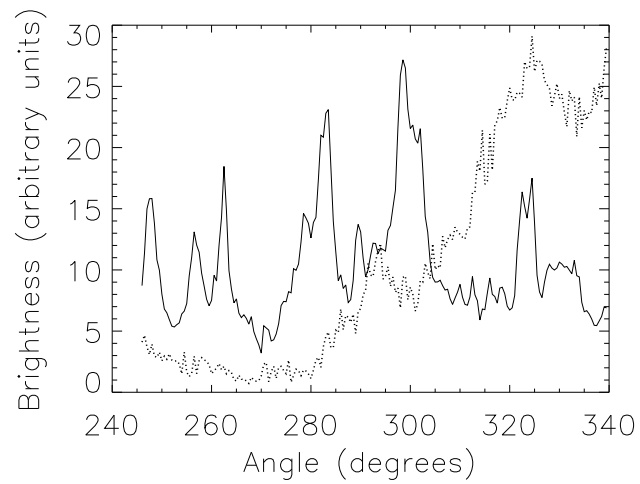


Fig. 3.— Comparison of X-ray continuum (solid) and radio (dotted) brightness along a 9'' wide circular arc of radius 220'', plotted against azimuthal angle measured counter-clockwise from north. One degree of azimuth corresponds to 3.8'' angular distance along the arc.

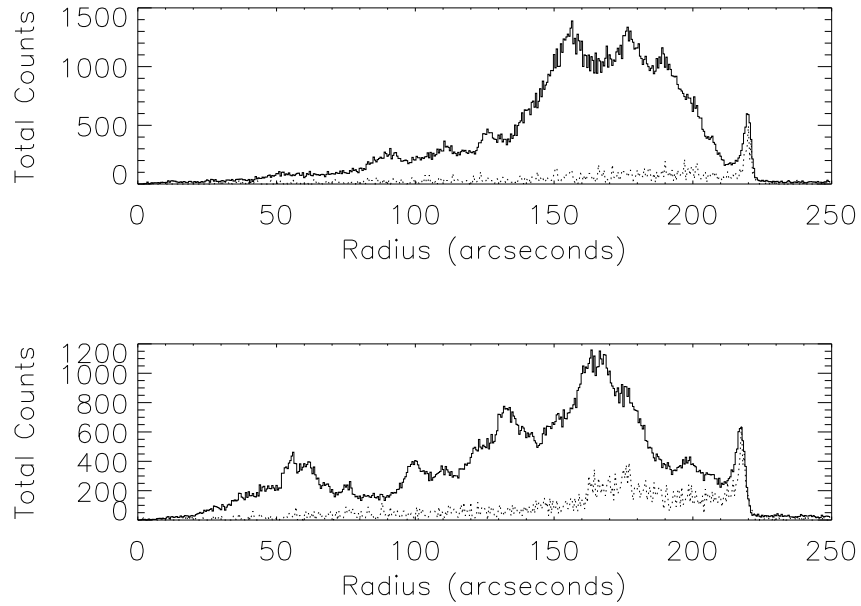


Fig. 4.— Radial profiles ending in portions of the northwestern (top; towards region 5) and southwestern (bottom; towards region 1) rims. The solid lines show the profiles of the broadband image, and the dotted lines show the profiles of the continuum image, multiplied by a factor of 15.

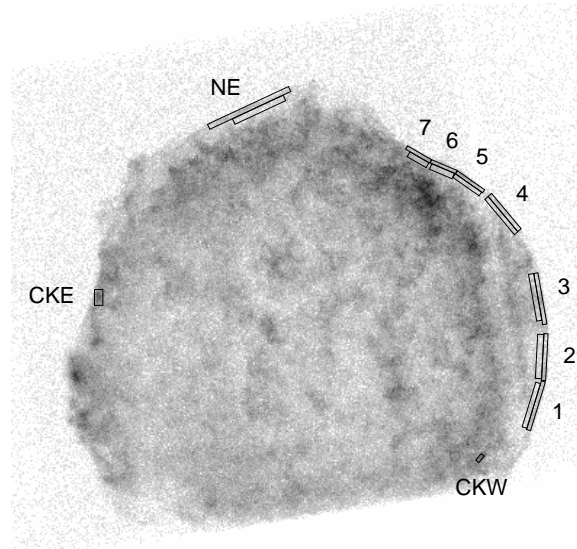


Fig. 5.— Chandra broadband image with the spectral extraction regions overlaid and labelled.

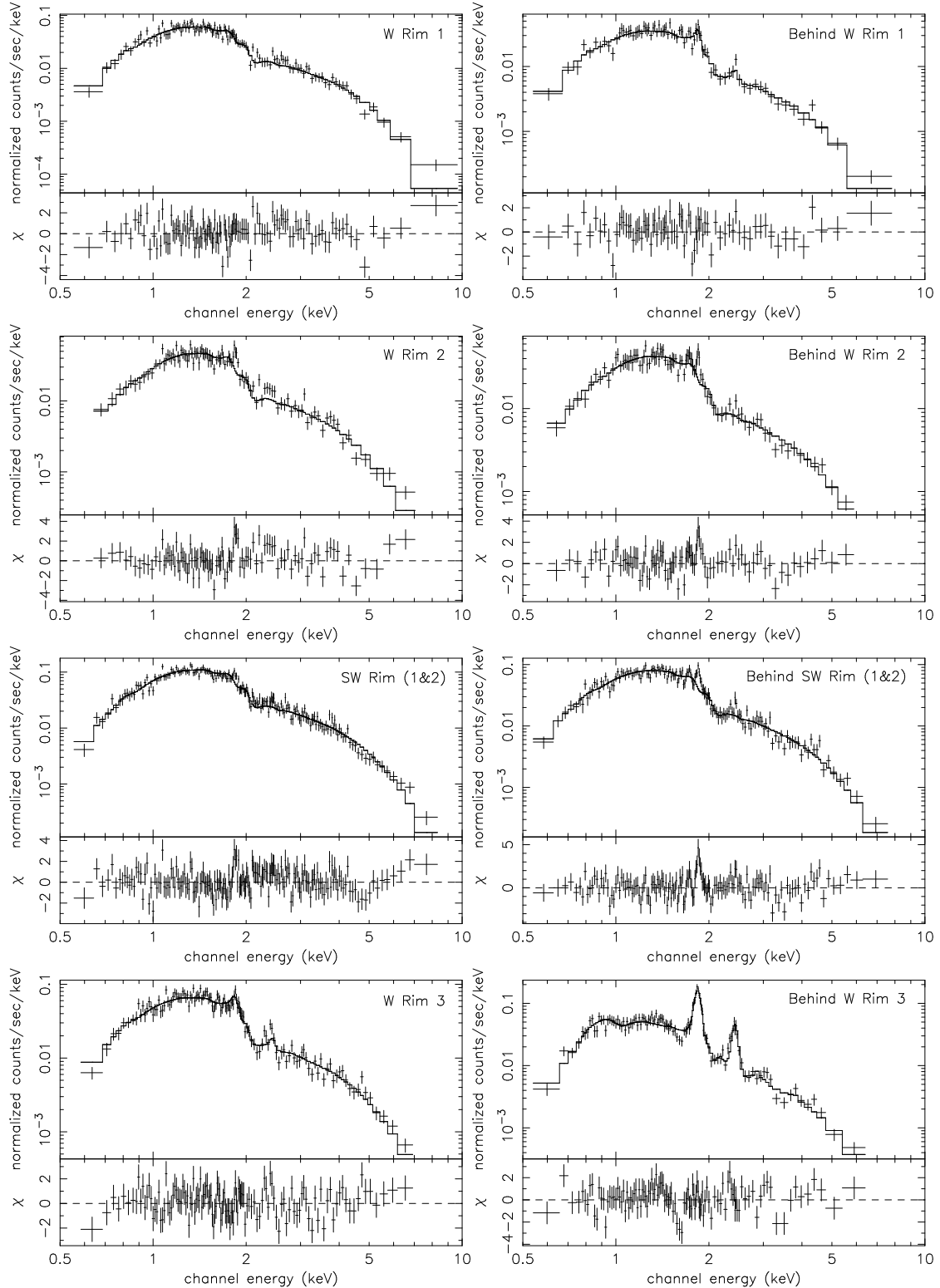


Fig. 6.—

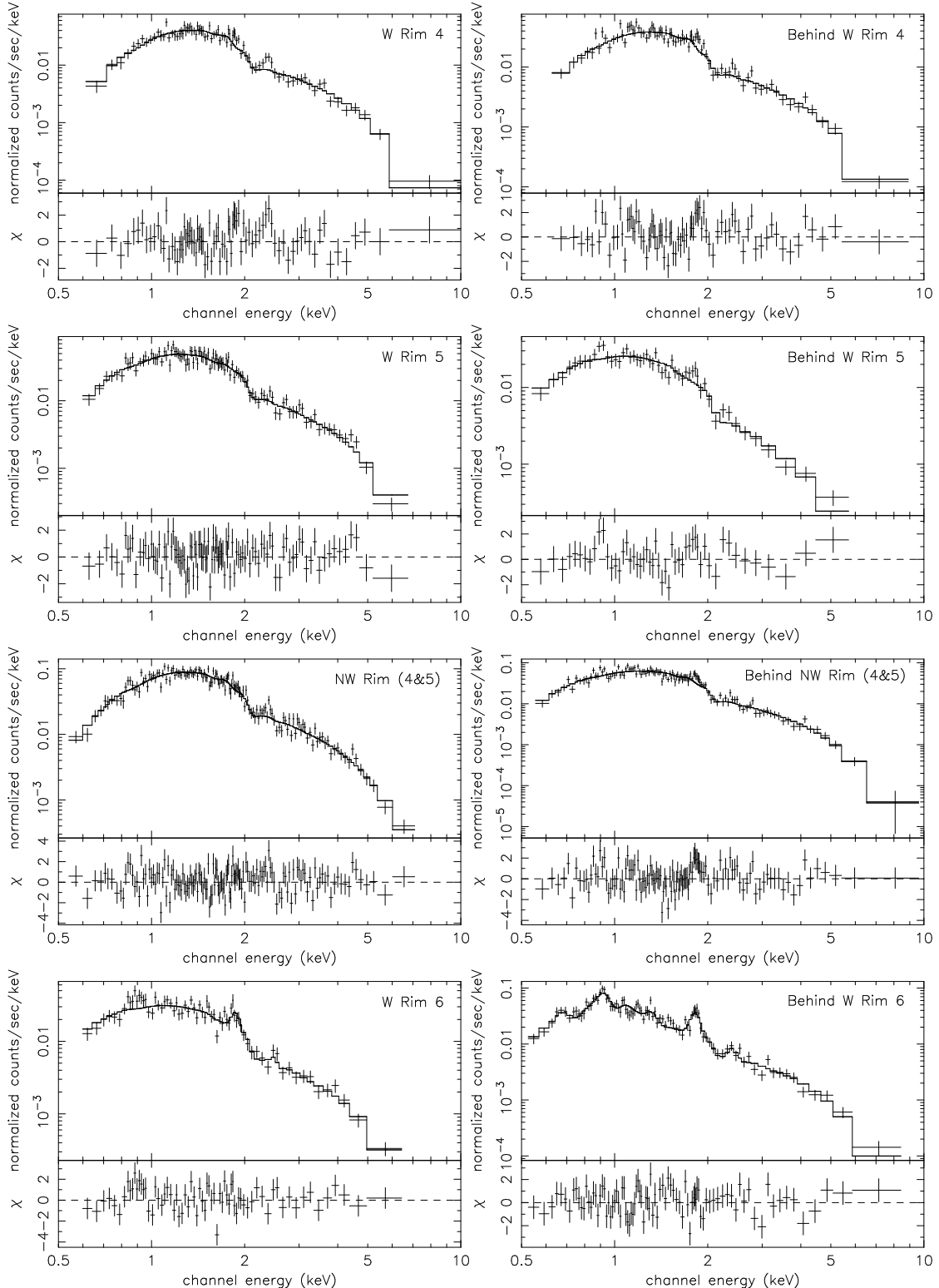


Fig. 6.—

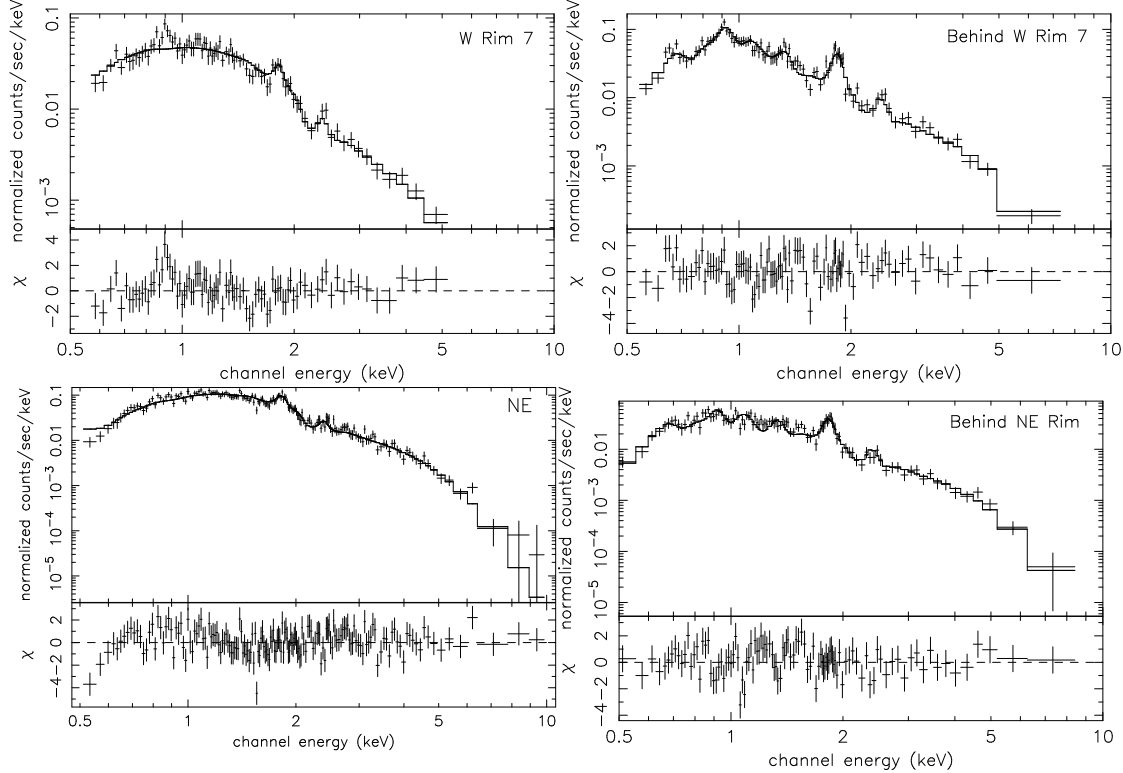


Fig. 6.— Spectra at and behind the rim shown with fitted thermal NEI models described in the text, starting from the SW (see Fig. 3) and progressing counterclockwise to the NE.

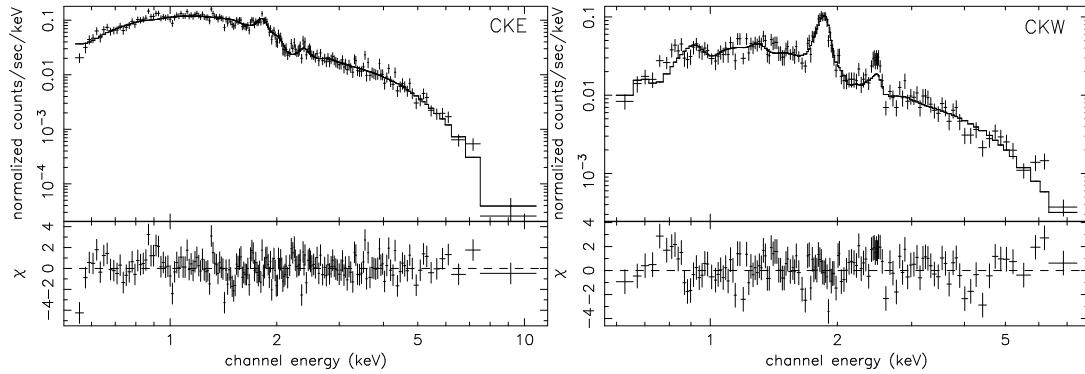


Fig. 7.— Spectra of the eastern and western hard continuum knots, with two-component NEI models representing forward shocked gas and reverse shocked ejecta.

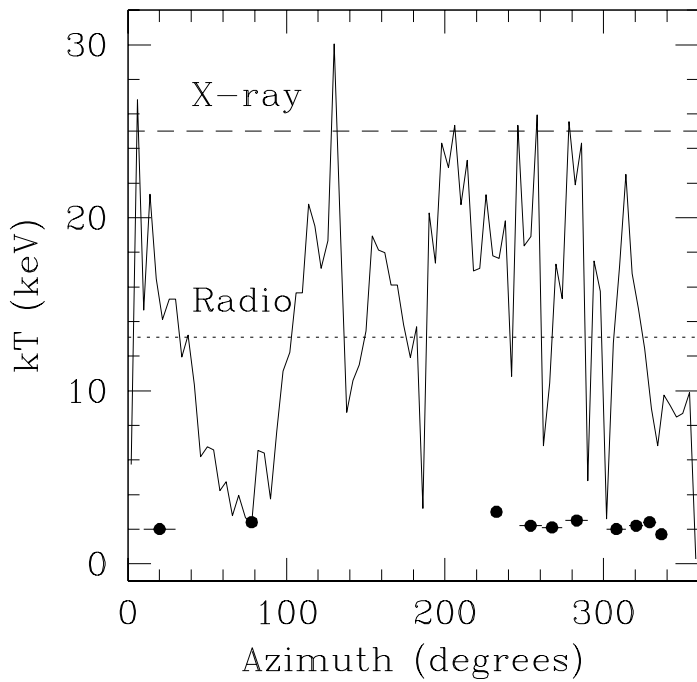


Fig. 8.— Equilibrium mean temperatures behind the shock front from radio shock velocities computed from Reynoso et al. (1997), plotted against azimuthal angle increasing counter-clockwise from north. The scatter in the south and southwest (angles greater than 200) is attributed to uncertainties in the radio expansion from uncertainties in obtaining the radius. The dotted line shows the temperature corresponding to the mean radio expansion, and the dashed line shows the temperature corresponding to the mean X-ray expansion from Hughes (2000). The measured electron temperatures at the rim from Table 4 and the two hard knots from Table 5 are plotted as the data points starting with the NE, CKE, CKW, and on through the rim regions 1 through 7. The temperature error bars are smaller than the data points, and the angular extent of the spectral extraction region is indicated by the horizontal bars.

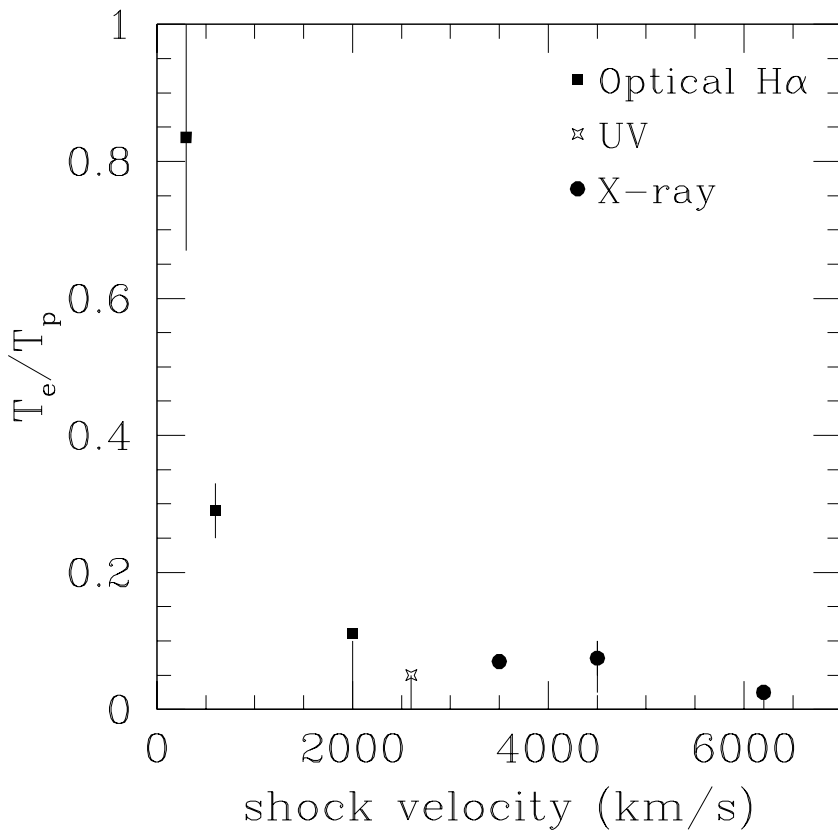


Fig. 9.— Ratios of electron and proton temperatures inferred for supernova remnant shocks at various wavelengths. Given in order of increasing shock velocity, optical results for non-radiative shocks in the Cygnus Loop, RCW 86, and Tycho's SNR are shown as the squares and are taken from Ghavamian et al. (2001); the UV result for SN 1006 are shown as a star and are from Laming et al. (1996); the X-ray results are shown as circles for SN 1987A from Michael et al. (2002) using mean mass per particle of 0.7; for Tycho's SNR from this work, and E0102-72 from Hughes et al. (2000) using a mean mass per particle of 0.6.

Table 1. Energy Band Images

	Pulse Height*	Raw Counts
Total	1-1024	5.5×10^6
Fe L	46-65	1.3×10^6
Si	112-135	1.8×10^6
Continuum	276-424	50,000
Fe K	428-451	7,000

*Nominal energies are obtained from the pulse heights, which are corrected for the spatial variation in the gain, as energy in eV = pulse height $\times 14.6$.

Table 2. Regions

Region	Cnts	Length*	Width*
Rim 1 (SW)	4281	110	9
Behind 1 (SW)	2587	100	11
Rim 2 (SW)	3379	101	9
Behind 2 (SW)	3045	95	13
Rim 3	5020	112	9
Behind 3	4600	102	11
Rim 4 (NW)	2829	99	10
Behind 4 (NW)	2732	99	10
Rim 5 (NW)	3568	71	8
Behind 5 (NW)	1834	69	10
Rim 6	2415	59	8
Behind 6	3269	53	13
Rim 7	3249	59	8
Behind 7	3760	47	12
Rim NE	8171	192	12
Behind NE	3228	120	13

*Dimensions are given in pixels, which are 0.5''.

Table 3. Northwest Rim (4+5): Spectral Fits

Model	$\chi^2, \chi^2/dof$	N_H (10^{22} cm^{-2})	kT or α^a (keV or –)	$n_e t$ or ν^b ($\text{cm}^{-3} \text{ s or Hz}$)	Normalization
bremsstrahlung	179.9, 1.28	0.53 (0.50-0.56)	2.1 (2.0-2.2)	–	6.2e-4 (5.8-6.7e-4)
parallel shock	179.6, 1.28	0.53 (0.50-0.56)	2.1 (1.9-2.2)	1.1e8 ($<3.5\text{e}8$)	1.9e-3 (1.8-2.1e-3)
NEI	179.6, 1.28	0.53 (0.50-0.56)	2.1 (1.9-2.2)	1.0e8 ($<2.3\text{e}8$)	..
power-law	217.9, 1.55	0.75 (0.71-0.79)	2.79 (2.71-2.87)	–	7.8e-4 (7.1-8.4e-4)
srcut	199.4, 1.41	0.66 (0.63-0.69)	0.52 (0.51-0.53)	7.0e16 (5.4-8.4e16)	[0.086] ^c
	201.5, 1.43	0.68 (0.65-0.70)	[0.72]	1.1e17 (0.90-1.4e17)	2.8 (2.5-3.6)
srcut+NEI	179.6, 1.29	0.53 (0.52-0.62)	$\alpha=0.52$ $kT=2.1$ (1.9-2.2)	$\nu=1.4\text{e}15$ (1.0e10-2.5e16) $nt=1.0\text{e}8$ ($<1.8\text{e}8$)	[0.086] 1.9e-3 (1.5-2.1e-3; $>75\%$ of flux)

^aTemperature kT is given for bremsstrahlung, parallel shock, and NEI models, spectral index α in X-rays for power-law, and in radio for *srcut* models. Please see the text for further discussion.

^bIonization age $n_e t$ is given for planar shock and NEI models, rolloff frequency ν for nonthermal *srcut* models.

^cIn this and other tables, quantities in square brackets are held fixed at the value given.

Table 4. Rim: Spectral Fits with Thermal *NEI* Models

Region	$\chi^2, \chi^2/dof$	N_H (10^{22} cm^{-2})	FS: kT (keV)	$n_e t$ ($\text{cm}^{-3} \text{ s}$)	RS [†] : kT (keV)	$n_e t$ ($\text{cm}^{-3} \text{ s}$)	Fe (rel \odot)
Rim 1	135.8, 1.18	0.60 (0.56-0.64)	2.2 (2.0-2.3)	1.0e8 (<2.2e8)	–	–	–
Behind 1	68.5, 0.94	0.46 (0.42-0.52)	1.9 (1.7-2.1)	1.0e8 (<2.5e8)	[0.9]	1.2e11 (3.4e10-9.0e11)	[0]
Rim 2	140.6, 1.42 [‡]	0.63 (0.57-0.68)	2.1 (2.0-2.3)	3.2e8 (<4.3e8)	–	–	–
Behind 2	95.7, 1.10	0.51 (0.45-0.57)	2.0 (1.8-2.2)	2.5e8 (<3.5e8)	–	–	–
SW Rim (1-2)	206.7, 1.18	0.61 (0.58-0.65)	2.1 (2.0-2.2)	1.0e8 (<2.2e8)	–	–	–
Behind SW	209.2, 1.44	0.51 (0.47-0.55)	1.9 (1.8-2.0)	1.8e8 (<2.6e8)	–	–	–
Rim 3	150.0, 1.19	0.48 (0.44-0.51)	2.6 (2.4-2.8)	1.0e8 (<2.0e8)	[0.9]	1.4e11 (< 6.9e11)	[0]
Behind 3*	132.8, 1.24	0.52 (0.47-0.62)	2.0 (1.8-2.2)	1.0e8 (<2.1e8)	[0.9]	8.1e10 (5.6e10-1.1e11)	0.04 (0.03-0.05)
Rim 4	89.1, 1.13	0.57 (0.52-0.63)	2.0 (1.8-2.1)	1.0e8 (<2.7e8)	–	–	–
Behind 4	108.3, 1.39 [‡]	0.46 (0.41-0.52)	2.0 (1.8-2.2)	1.8e8 (<3.1e8)	–	–	–
Rim 5	97.0, 0.95	0.49 (0.45-0.53)	2.2 (2.0-2.4)	1.0e8 (<2.5e8)	–	–	–
Behind 5	51.7, 1.08	0.29 (0.26-0.34)	1.6 (1.4-1.9)	1.0e8 (<1.7e8)	–	–	–
NW Rim (4-5)	179.4, 1.28	0.53 (0.50-0.56)	2.1 (1.9-2.2)	1.0e8 (<2.2e8)	–	–	–
Behind NW	145.4, 1.25	0.39 (0.36-0.42)	1.9 (1.8-2.1)	1.0e8 (<3.0e8)	–	–	–
Rim 6	84.9, 1.31	0.28 (0.24-0.31)	2.4 (2.1-2.8)	1.0e8 (<2.1e8)	[0.9]	1.6e11 (>1.2e10)	[0]
	69.2, 1.08	0.52 (0.38-0.74)	2.2 (1.8-2.5)	4.3e8 (2.6-6.4e8)	[0.9]	4.9e10 (3.3-7.3e10)	0.27 (0.11-0.92)
Behind 6	104.7, 1.23	0.84 (0.82-0.88)	2.5 (2.3-2.9)	2.5e9 (1.9-3.0e9)	[0.9]	6.2e10 (4.8-8.3e10)	1.2 (0.8-2.1)
Rim 7	96.8, 1.17	0.24 (0.21-0.27)	1.7 (1.5-1.9)	1.0e8 (<1.4e8)	[0.9]	5.3e9 (3.2-7.7e9)	[0]
Behind 7	119.0, 1.31	0.88 (0.85-0.91)	2.0 (1.8-2.2)	3.3e9 (2.9-3.7e9)	[0.9]	8.9e10 (6.5e10-1.3e11)	0.8 (0.6-1.1)
NE Rim	202.9, 1.23	0.44 (0.42-0.46)	2.0 (1.9-2.1)	1.0e8 (<1.2e8)	[0.9]	6.3e9 (4.5-8.8e9)	[0]
Behind NE	116.9, 1.16	0.95 (0.92-0.97)	2.1 (1.9-2.3)	3.5e9 (3.2-3.9e9)	[0.9]	4.8e10 (1.6e10-4.9e11)	[0]

[†]Please see the text for discussion of the reverse shocked ejecta component.

[‡]Addition of an ejecta component improves the fit substantially, but is poorly constrained.

*The S abundance was freely fitted to be 2.1 (1.7-2.5) relative to its solar value.

Table 5. Rim: Spectral Fits with Nonthermal *srcut* Models

Region	$\chi^2, \chi^2/dof$	N_H (10^{22} cm^{-2})	Fitted α	Radio α^a	Radio Flux ^b (Jy)	ν^c (Hz)
NE ^d	211.2, 1.27	0.58 (0.57-0.60)	[0.55]	0.55 ± 0.04	[0.21]	5.2e16 (5.1-5.3 e16)
NW (4&5)	199.4, 1.41	0.66 (0.63-0.69)	0.52 (0.51-0.53)	0.72 ± 0.14	[0.086]	7.0e16 (5.4-8.4e16)
SW (1&2)	259.5, 1.47	0.87 (0.85-0.90)	[0.40]	0.40 ± 0.15	[0.03]	3.3e16 (3.2-3.4e16)
	228.2, 1.30	0.76 (0.73-0.78)	0.440 ± 0.005	0.40 ± 0.15	[0.03]	5.8e16 (5.0-7.1e16)

^aRadio spectral index α as given by Katz-Stone et al. (2000).

^bRadio flux at 1 GHz (please see the text).

^cRolloff frequency of the spectrum.

^dThe model for this spectrum also includes an ejecta component with kT fixed at 0.9 keV and $nt = 7.6e9$ (5.5e9-1.0e10) for Si and S in their solar abundance ratios.

Table 6. Hard Continuum Knots: Spectral Fits

Region	$\chi^2, \chi^2/dof$	N_H (10^{22} cm^{-2})	FS: kT (keV)	$n_e t$ ($\text{cm}^{-3} \text{ s}$)	RS: kT (keV)	$n_e t$ ($\text{cm}^{-3} \text{ s}$)
CKE	226.9, 1.22	0.30 (0.28-0.31)	3.3 (3.0-3.5)	1.e8 (<1.3e8)	[0.9]	5.3e9 (3.9-7.1e9)
CKW	221.9, 1.64	1.13 (1.08-1.19)	3.0 (2.6-3.3)	3.0e9 (2.7-3.3e9)	[0.9]	1.3e11 (7.4e10-2.7e11)